



HAL
open science

Auger recombination and multiple exciton generation in colloidal two-dimensional perovskite nanoplatelets: Implications for light-emitting devices

Carolina Villamil Franco, Benoit Mahler, Christian Cornaggia, Thomas Gustavsson, Elsa Cassette

► To cite this version:

Carolina Villamil Franco, Benoit Mahler, Christian Cornaggia, Thomas Gustavsson, Elsa Cassette. Auger recombination and multiple exciton generation in colloidal two-dimensional perovskite nanoplatelets: Implications for light-emitting devices. *ACS Applied Nano Materials*, 2021, 4 (1), pp.558-567. 10.1021/acsanm.0c02868 . hal-03175975

HAL Id: hal-03175975

<https://hal.science/hal-03175975>

Submitted on 5 Oct 2021

HAL is a multi-disciplinary open access archive for the deposit and dissemination of scientific research documents, whether they are published or not. The documents may come from teaching and research institutions in France or abroad, or from public or private research centers.

L'archive ouverte pluridisciplinaire **HAL**, est destinée au dépôt et à la diffusion de documents scientifiques de niveau recherche, publiés ou non, émanant des établissements d'enseignement et de recherche français ou étrangers, des laboratoires publics ou privés.

1
2
3
4
5
6
7 Auger Recombination And Multiple Exciton Generation
8
9
10
11 In Colloidal Two-Dimensional Perovskite
12
13
14 Nanoplatelets: Implications For Light-Emitting Devices
15
16
17

18
19 *AUTHOR NAMES. Carolina Villamil Franco¹, Benoît Mahler², Christian Cornaggia¹, Thomas*
20
21 *Gustavsson¹ and Elsa Cassette^{1,*}*
22
23

24
25
26
27 AUTHOR ADDRESS. ¹Université Paris-Saclay, CEA, CNRS, Laboratoire Interactions,
28
29 Dynamiques et Lasers (LIDYL), 91191 Gif-sur-Yvette, France. ²Université de Lyon, Université
30
31 Claude Bernard Lyon 1, CNRS, Institut Lumière Matière (ILM), F-69622 Villeurbanne, France.
32
33

34
35
36
37
38 KEYWORDS. Halide perovskite, quantum confinement, Auger recombination, multiple
39
40 exciton generation, 2D nanoplatelets
41
42
43
44
45
46
47
48
49
50
51
52
53
54
55
56
57
58
59
60

1
2
3 ABSTRACT. Improving the understanding of multiple exciton interactions and dynamics in
4 semiconductor nanostructures is mandatory for their successful use as photoactive materials in
5 light convertors such as electroluminescent diodes (LEDs), lasers or single-photon sources.
6 Here high-fluence and high-energy excitation effects are investigated in strongly confined two-
7 dimensional lead iodide perovskite nanoplatelets using time-resolved photoluminescence and
8 femtosecond transient absorption spectroscopy. Non-radiative Auger recombination is the
9 dominant pathway for multiexciton recombination. Its dynamics is found to be sub-quadratic
10 with the exciton density. Indeed, due to the limited exciton wavefunction delocalization length,
11 the Auger recombination is limited by the exciton diffusion in the two-dimensional plane at
12 moderate excitation fluence and takes place in several hundreds of picoseconds, with typical
13 recombination rates in the order of 10^{-2} cm²/s. At high excitation fluence leading to an average
14 inter-exciton distance comparable with the exciton delocalization length, the measured
15 “intrinsic” Auger recombination time is faster than 10 ps and independent of the nanoplatelet
16 composition. The strong dependency of the Auger recombination rate on the inter-exciton
17 distance allows us to identify the recombination resulting from multiple exciton generation,
18 involving the reaction of “geminate biexcitons”, when exciting at low fluence with high-energy
19 photons.
20
21
22
23
24
25
26
27
28
29
30
31
32
33
34
35
36
37
38
39
40
41
42
43
44
45
46
47
48
49
50
51
52
53
54
55
56
57
58
59
60

INTRODUCTION

By combining strong photoluminescence, color purity and enhanced stability with easy and cheap solution-processing fabrication, two-dimensional (2D) halide perovskites have taken a central role in the development of electroluminescent diodes (LEDs), laser gain media or single-photon sources.¹⁻³ For all these various light-emitting devices, understanding the exciton-exciton annihilation process, which ultimately limits the exciton density in these materials, is essential in order to control the device performances. For example, lasing threshold and LED efficiency are affected by the rapid non-radiative Auger recombination (AR) rate that limits the maximum electron-hole pair density in the photoactive material.⁴ It is well established that AR is the dominant recombination process that occurs in semiconductor nanostructures under high-excitation density.^{5,6}

Over the last few years, AR has been the subject of several investigations in weakly-confined colloidal perovskite nanocrystals (NCs).⁷⁻⁹ However, studies in strongly confined 2D perovskite samples are limited to a few cases: methylammonium lead iodide (MAPI) 2D layered thin films^{10,11} and 5 monolayers (MLs) CsPbBr₃ nanoplatelets (NPLs).^{12,13} While an increase of the AR rate is expected with the increase of the Coulomb interactions in confined systems, a surprisingly slow “bimolecular” AR rate of a few 10⁻⁴ and 10⁻³ cm²/s was reported in 2D perovskite films in the strong confinement regime (1 to 5 MLs), leading to effective AR times on the order of hundreds of picoseconds to nanoseconds.^{10,11} Interestingly, in a recent publication a decrease from 78 ps to 18 ps was reported in the effective biexcitonic recombination time of weakly-confined CsPbI₃ NCs (size 12.1 nm) compared to in more-strongly confined ones (6.2 nm).¹⁴ Depending on the nature of the photoexcited species (free charge carrier or excitons), the AR process will follow third-or second-order kinetics.^{15,16} Besides, the anisotropic geometry of a system like the 2D quantum wells can induce further

1
2
3 modifications in the measured kinetics such as asymmetric exciton-exciton interactions¹⁷ and
4
5 diffusion-limited recombination.^{11,18}
6

7
8 Here, we studied the multiple exciton dynamics in strongly-confined lead iodide colloidal NPLs
9
10 of 2 and 3 MLs by varying the excitation fluence from less than one to tens of $\mu\text{J}/\text{cm}^2$. We found
11
12 a fast intrinsic AR rate with a corresponding effective recombination time of less than 10 ps at
13
14 high exciton density ($> 5 \times 10^{11} \text{ cm}^{-2}$) while exciton diffusion slows down the AR process to
15
16 hundreds of ps when the initial exciton density is low.
17
18

19
20 We also studied the formation of multiple excitons in these NPL samples by observing the AR
21
22 that occurs after high photon energy and low fluence excitation. So far, multiple exciton
23
24 generation (MEG) has only been observed in weakly-confined iodide-based perovskite
25
26 nanocrystals, CsPbI_3 , and FAPbI_3 , using transient absorption spectroscopy.^{14,19,20} These
27
28 measurements are always very sensitive to photo-charging effects and/or a misinterpretation as
29
30 a result of a too high excitation fluence.²¹ Surprisingly, Klimov and coworkers did not observed
31
32 any MEG signatures in Cs-based perovskite NCs using time-resolved photoluminescence (TR-
33
34 PL) techniques.⁷ Here, we show that MEG induces a fast AR rate in 3 ML-thick NPLs due to
35
36 the proximity of the two “geminate” excitons, that can be easily isolated from other non-
37
38 radiative recombinations.
39
40
41
42

43 44 EXPERIMENTAL SECTION

45
46
47 **Perovskite Nanoplatelets synthesis.** All the commercially available chemicals used for the
48
49 synthesis of colloidal perovskite nanostructures are listed in the Supporting Information (SI).
50
51 Thin perovskite nanoplatelets were synthesized at room temperature by precipitation by
52
53 injecting the precursor solution into a non-polar solvent, here the toluene (see full details in the
54
55 SI).
56
57
58
59
60

1
2
3 **Steady-state optical characterization.** Absorption measurements were carried out with a
4 UV/Vis Lambda 850 spectrophotometer (Perkin Elmer) covering the 175-900 nm spectral
5 range. Photoluminescence was carried out with a Fluorolog 3-22 spectrofluorometer (HORIBA
6 JOBIN-YVON) equipped with a R928P photomultiplier tube detector (200-870 nm) and a CW
7 Xenon arc lamp (450 W, 250-2500 nm). A UV enhanced silicon photodiode reference detector
8 monitors and compensates for variation in the Xenon lamp intensity.
9

10 **Time-correlated single photon counting (TCSPC).** We used a mode-locked Ti:Sapphire
11 (MIRA 900, Coherent) pumped by a solid state laser (VERDI V10, Coherent) and providing
12 120 fs pulses tunable between 720 and 950 nm (about 2 W at 800 nm), at 76 MHz repetition
13 rate. The rate was reduced to 200 kHz using a pulse picker (Model 9200, Coherent). The output
14 pulse train was subsequently frequency-doubled, providing 400 nm pulses. The polarization of
15 the excitation beam was controlled by a Fresnel rhomb (EKSMA) and set parallel to the
16 detection. The fluorescence was collected on a monochromator (HR250, Jobin-Yvon). A Schott
17 WG 420 filter was positioned in front of the entrance slit in order to cut the diffused excitation
18 light. The fluorescence was detected with a microchannel plate photomultiplier (R1564 U,
19 Hamamatsu). The temporal resolution is about 60 ps with a time window < 100 ns. To avoid
20 photodegradation, the samples were continuously refreshed using a circulating system and a
21 stirred bar in a 3 mm quartz cell.
22
23
24
25
26
27
28
29
30
31
32
33
34
35
36
37
38
39
40
41
42
43
44
45

46 **Transient Absorption (TA).** All measurements of the colloidal perovskite nanostructures were
47 carried out at room temperature in a 1 mm-thick flow cell connected to a peristaltic pump in
48 order to refresh the sample at the focus position to avoid photodamage and photocharging
49 effects. Flexible and organic solvent compatible F-5500-A fluoroelastomer (Saint-Gobain®)
50 tubing and Teflon adaptors were used to build the flow system. The employed sample solutions
51 were prepared with optical density (OD) below 0.3 at the excitation wavelength and above in
52 anhydrous toluene (or chloroform). We used a home-built TA fs spectrometer with an initial
53
54
55
56
57
58
59
60

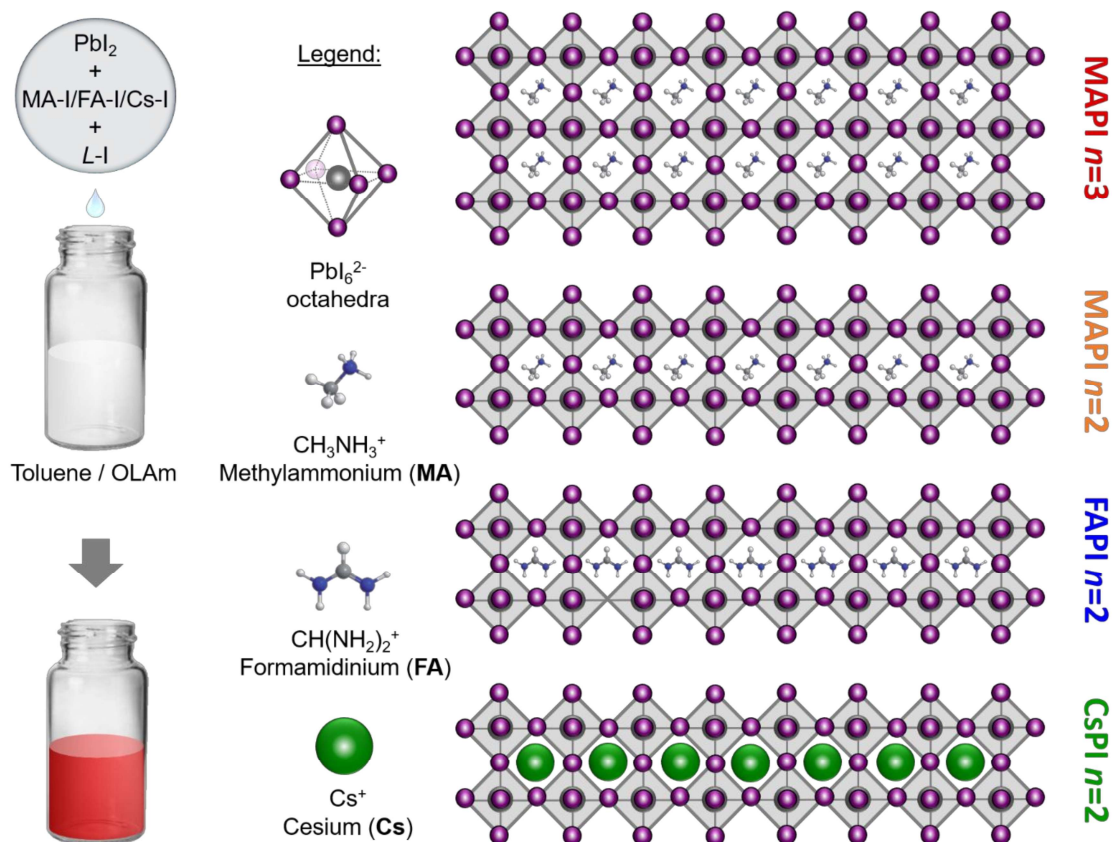
1
2
3 Ti:Sa laser source at 3 kHz, 40 fs and about 2 W to generate a tunable excitation in the 500-650
4 nm range with a non-collinear optical parametric amplifier (NOPA) and a white-light (WL)
5 continuum for the probe. The output of the NOPA, after a temporal compression involving
6 chirped mirror pair and a double-prism compressor, can be frequency doubled using a set of
7 lens, a BBO crystals and polarizers to filter out the residual visible beam. The temporal
8 resolution is about 100 fs in the visible and about 300 fs for the UV experiments. The maximum
9 pump-probe time delay that can be reached is about 3.2 ns using a long delay line with a
10 retroreflector mounted on a motorized stage (60 cm long, minimum step 200 nm,
11 IMS600CCHA from Newport). The continuum probe beam was filtered to remove the
12 fundamental 800 nm and reduced in intensity by a neutral density filter. Both pump and probe
13 were set vertical in polarization using broadband half-waveplates. The repetition rate of the
14 pump is reduced to half (1.5 kHz) to block one pulse out of two, allowing for measures with
15 and without the pump.
16
17
18
19
20
21
22
23
24
25
26
27
28
29
30
31
32

33 The continuum spectrum was registered at 3 kHz by a commercial spectrograph (IsoPlane 160,
34 Princeton Instruments) coupled to a CCD camera (ProEM-HS 1024B, Princeton Instruments).
35
36

37 To measure a spectrum of 1024 pixels at 3 kHz with the CCD camera (3000 frames/s), we use
38 a fast-custom acquisition mode with a vertical binning of 64 pixels (13 μm each) over the region
39 of interest (ROI) closest to the chip and an exposure time of 1 μs . The TA signal was calculated
40 as follow: $\Delta A(\lambda, t) = -\log\left(\frac{1}{m}\sum_{k=0}^{m-1} \frac{I_{2k}^{ON}(\lambda, t) - I_{fluo}(\lambda)}{I_{2k+1}^{OFF}(\lambda, t) - I_{dark}(\lambda)}\right)$, with $I(\lambda, t)$ the WL spectrum measured
41 at a pump-probe time delay t with the pump “ON” for a pulse $2k$ (even) and the pump OFF for
42 the following pulse $2k+1$ (odd), I_{fluo} the spectrum recorded with the probe beam blocked, I_{dark}
43 the spectrum measured with both pump and probe blocked and m the number of ON/OFF
44 kinetic cycle pairs to average at one position of the translation state (for each different t). Both
45 I_{fluo} and I_{dark} correspond to background spectra that need to be subtracted before performing the
46
47
48
49
50
51
52
53
54
55
56
57
58
59
60

ratio of the WL spectrum. They are collected just before the scan collection, averaged over 3000 pulses.

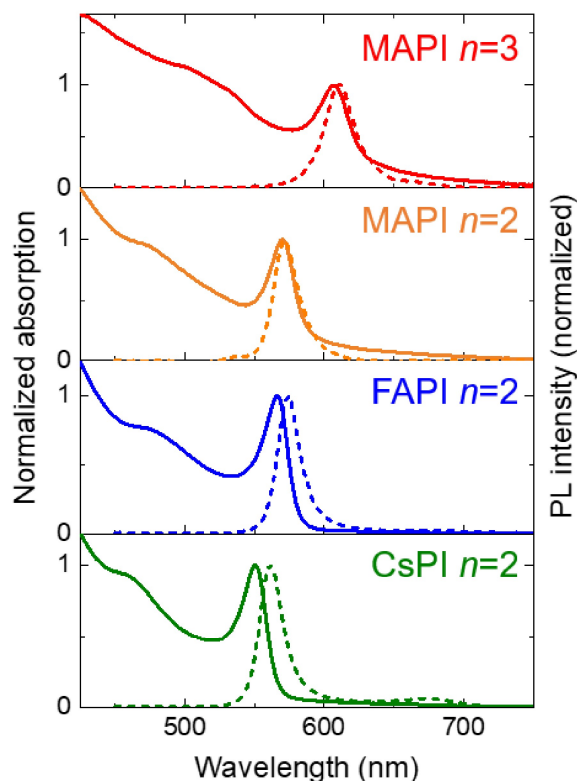
RESULTS AND DISCUSSION



Scheme 1. Schematics of the lead iodide perovskite NPL samples and their colloidal synthesis (L = ammonium ligand, OLAm = oleylamine).

Nanoplatelet sample characterizations. Colloidal perovskite NPLs were synthesized at room temperature based on the ligand assisted re-precipitation (LARP) method²² (Scheme 1, details in EXPERIMENTAL SECTION and SI). From the initial report of two-monolayer-thick $L_2[\text{APbI}_3]\text{PbI}_4$ ($n=2$ MAPI, FAPI and CsPI) NPLs with L , an ammonium ligand and A an inorganic (cesium, Cs) or organic (methylammonium, MA or formamidinium, FA) cation, we extended the synthesis to three-monolayer-thick $L_2[\text{MAPbI}_3]_2\text{PbI}_4$ NPLs (MAPI $n=3$). The

1
2
3 schematics of the different samples is shown in **Scheme 1**. Unlike the ligand-assisted
4
5 exfoliation procedures used in previously reported hybrid colloidal NPLs,^{23,24} the direct
6
7 solution approach allows a more well-defined population (*i.e.* number of monolayers) in thinner
8
9 NPLs.
10
11
12



41
42 **Figure 1.** Absorption (full line) and photoluminescence (dashed line) spectra of colloidal
43
44 perovskite NPLs of two monolayers (CsPI, FAPI, MAPI $n=2$) and three monolayers (MAPI
45
46 $n=3$).
47

48
49 The steady-state absorption and photoluminescence (PL) spectra of the synthesized NPLs
50
51 dispersed in toluene are shown in **Figure 1**. For each sample, the energy corresponding to the
52
53 first exciton transition matches the previous reports of strongly confined 2D NPLs and thin
54
55 films^{25–27}. Except for CsPI $n=2$, all NPL samples present lateral dimensions from hundreds of
56
57 nanometers to a few micrometers (see SI) and thus confinement in these dimensions can be
58
59
60

neglected. The CsPI sample, however, might display some degree of confinement in one of the lateral dimensions (nanoribbons with a width of 17 ± 3 nm and a length of several hundreds of nm, see **Figure S1** in SI). While the small blue shift in the spectrum of Cs-based perovskite samples compared to MA- and FA-based ones is typical,²⁸ here it might be the consequence of the extra confinement effects, which could affect the AR rate.¹²

Time resolved photoluminescence experiments. TR-PL is a standard method to study multi-exciton dynamics in colloidal nanostructures. Since the PL signal is proportional to the average number of bound electron-hole pairs in the excited nanoparticles, which allows to distinguish different kinetic recombination processes.²⁹ Here, we employ the time-correlated single-photon counting (TCSPC) technique (see EXPERIMENTAL SECTION) with an instrument response function (IRF) of about 60 ps, to record luminescence decays of the four colloidal perovskite NPLs at the band-edge after excitation at 400 nm. By varying the excitation fluence from 40 nJ/cm² to 15 μ J/cm², multiexciton interactions may be revealed.

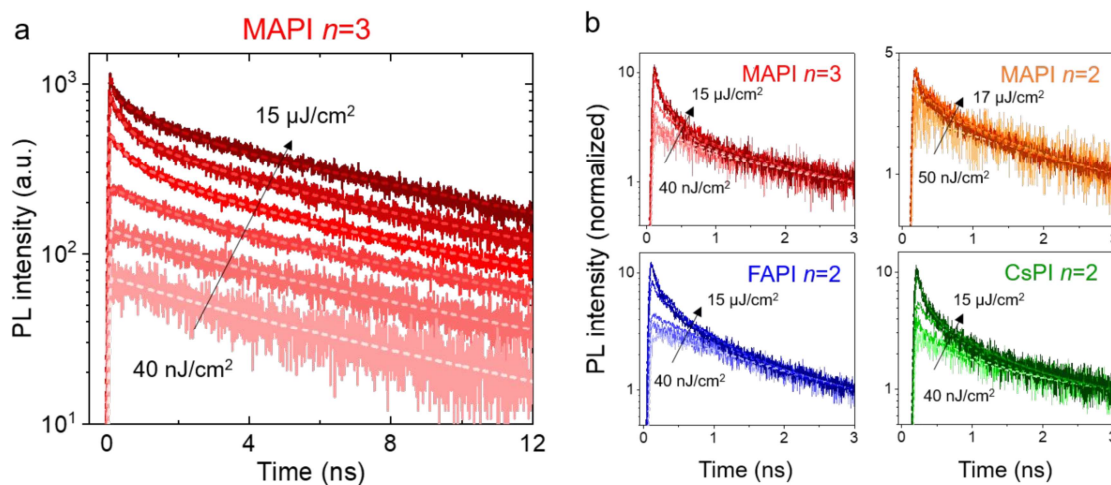


Figure 2. Fluence-dependent PL decay traces of the perovskite NPLs excited at 400 nm (bandedge detection). **(a)** Experimental data (full lines) and fit (dashed lines) for MAPI *n*=3 NPLs. **(b)** Experimental data and fit of the four different NPL samples normalized at long time to highlight the extra decay at early time at high excitation fluence.

1
2
3 The PL decay traces recorded for MAPI $n=3$ at different excitation fluences at 400 nm are
4 shown in **Figure 2a**. The data for the $n=2$ NPL samples are displayed in **Figure S2** in the SI.

7 The PL decay traces could be well fitted by a multiexponential function. All the corresponding
8 fit parameters are given in the SI **Tables S1-S4**.

11 At low excitation fluencies, the dynamics are almost mono-exponential for MAPI and FAPI
12 NPLs, but a better description is obtained for all the samples using a biexponential decay
13 function, having time constants τ_2 and τ_3 . Starting at about $2 \mu\text{J}/\text{cm}^2$ (see the calculation of the
14 excitation fluences in the SI), an extra short-lived component appears, characterized by a time
15 constant τ_1 that decreases from a few hundreds to a few tens of ps with increasing excitation
16 fluence. At the same time, the middle component τ_2 decreases from just below (or few ns) to a
17 few hundreds of ps. The long component τ_3 , however, remains almost constant and is 10 ± 1 ,
18 5.7 ± 0.1 , 3.2 ± 0.6 and 5.9 ± 0.1 ns for MAPI $n=3$, MAPI $n=2$, FAPI $n=2$, and CsPI $n=2$,
19 respectively.

22 The constant value of the long component τ_3 for all excitation fluences shows that the PL signal
23 detected at several ns is mainly associated to mono-exciton recombination. Indeed,
24 recombination of free charge carriers will lead to bimolecular recombination, as previously
25 observed in bulk halide perovskites.³⁰ The amplitudes associated with this long component
26 saturate much faster than the total amplitudes (*i.e.* intensity at time $t=0$), as seen in **Figure S3**
27 in the SI for MAPI $n=3$. This means that while a high excitation fluence can generate several
28 excitons within a single NPL, multiexciton recombinations are efficient enough to reduce the
29 dynamics at long times to single exciton recombination. The larger value of τ_3 for the $n=3$ NPL
30 sample can be explained by its larger fluorescence quantum yield (see SI).

33 The consistency of the long time dynamics due to mono-exciton recombination allows us to
34 normalize the PL decay traces at a long time and to isolate the extra faster decay component
35 appearing at larger excitation densities. We assigned this faster component to multiple exciton
36

1
2
3 dynamics (**Figure 2b**), in line with previous reports.^{8,31–33} The decrease of the corresponding
4
5 effective multiexciton decay times τ_1 and τ_2 with the initial number of created excitons is
6
7 expected for quadratic multi-exciton recombination (see discussion below). As these time
8
9 constants are on the order of hundreds to tens of ps, they correspond to non-radiative AR rather
10
11 than radiative biexcitonic recombination (see discussion in SI). Here, trion dynamics, which
12
13 corresponds to another kind of Auger recombination can be neglected since the samples were
14
15 circulated within the 3 mm-cell and the repetition rate decreased to 200 kHz to prevent from
16
17 photo-charging and photo-degradation effects.^{5,34}

18
19
20
21
22 If the main excited species are excitonic, AR follows bimolecular recombination kinetics:¹⁵

$$\frac{d\tilde{n}}{dt} = -\beta\tilde{n}(t)^2 \quad [1]$$

23
24
25
26
27 with $\tilde{n}(t)$ the time-dependent exciton density and β the “bimolecular” AR rate. For highly
28
29 asymmetric 2D nanostructures, the exciton density is surfacic (number of excitons N per NPL
30
31 surface, in cm^{-2}), such as β is typically displayed in cm^2/s . We note that a factor $\frac{1}{2}$ should
32
33 normally be added in front of β because, for relatively low excitation photon energy, the re-
34
35 excited exciton is not ionized and relax back to the band-edge at a cooling rate expected much
36
37 higher than the AR rate. We note however that this factor was not taken into account previously
38
39 so for a fair comparison we intentionally omit it.

40
41
42
43
44 The bimolecular Auger recombination requires a sufficiently high density of excitons to occur
45
46 since it involves *short-range* exciton-exciton interactions that are described either by a collision
47
48 process or a Förster energy transfer which scales as $(1/d_{X-X})^6$, where d_{X-X} is the distance between
49
50 the excitons (one exciton transfers its energy to re-excite the other exciton).³⁵ In the two limiting
51
52 cases of immobile excitons (*e.g.* self-trapped excitons)³⁶ and large exciton delocalization length
53
54 in the 2D plane (the wavefunction of the exciton center-of-mass motion extends well beyond
55
56 d_{x-x}^2),³⁷ β is constant in time and the solution to the **Equation 1** has the analytical form:¹⁵

$$\tilde{n}(t) = \frac{\tilde{n}(0)}{1 + \tilde{n}(0)\beta t} \quad [2]$$

with $\tilde{n}(0)$, the initial exciton density.

The measured PL intensity is proportional to the averaged instantaneous number of excitons $N(t)$ and thus to the corresponding density $\tilde{n}(t)$. We thus use the **Equation 2** to fit the isolated multiexciton PL decay traces, by fixing the initial exciton density $\tilde{n}(0)$ calculated from the excitation fluence and the linear absorption coefficient of the sample (**Figure S4a** in SI). The early-time TR-PL decay were well reproduced by the fit and we obtained an effective bimolecular AR rate β decreasing from 8.2×10^{-2} to 1.1×10^{-2} cm²/s with increasing excitation fluence from 0.15 to 15 $\mu\text{J}/\text{cm}^2$. These bimolecular AR rate values, listed in the first column of **Table S6** in the SI, are plotted against the exciton density in **Figure 3** (black squares). It is here worthwhile to note that the β values are orders of magnitude lower when using **Equation S2** in the SI to fit the full PL decay, including both multi- and single-exciton dynamics (second column of **Table S6** in SI), as reported by Huang and co. and Garrot and co..^{10,11} However, it is clear from the corresponding fits (**Figure S4b**), that these values are not representative of the multiexciton dynamics as the early time dynamics are not well reproduced. That is why we found important to fit the isolated multiexciton dynamics to extract the β values.

The experimental dynamics become faster when increasing the initial exciton density $\tilde{n}(0)$, which is in agreement with the effective linear AR rates, extracted from the multi-exponential fit, increasing with the excitation fluence (**Figure 3**, red dots). This expresses a super-linear dependency of the kinetics related to multi-exciton dynamics depending on the exciton density. As expected for a pure bimolecular recombination (*cf* **Equation 1 and 2**), the dynamics indeed become faster when increasing the initial exciton density. However, the corresponding bimolecular AR rate β should remain constant. The fact that the experimental β values extracted by bimolecular fits using **Equation 2**, decrease with the initial exciton density $\tilde{n}(0)$, shows that

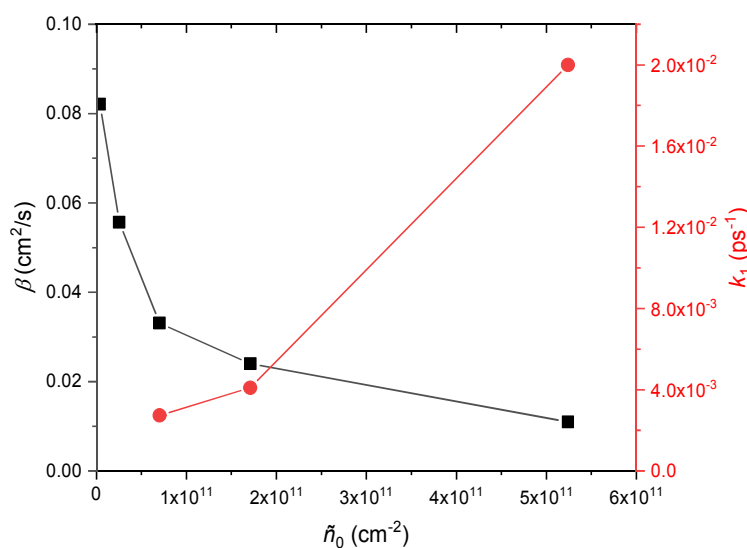
1
2
3 the isolated multi-exciton dynamics deviate from bimolecular kinetics. In particular, it shows
4
5 that the experimental kinetic dependency on \tilde{n} is sub-quadratic.
6

7
8 This trend can be understood if the bimolecular AR rate β in **Equation 1** is time-dependent.
9
10 This is for example the case if the bimolecular AR is limited by the exciton diffusion in the 2D
11
12 plane. In that case, the diffusion process reduces the dependency of the AR kinetics on the
13
14 exciton density \tilde{n} . Indeed, excitons initially separated by distances larger than the typical
15
16 reaction radius (*i.e.* moderated $\tilde{n}(0)$) will diffuse and eventually encounter, leading to an
17
18 effective recombination.
19
20

21
22 Several works on the exciton-exciton annihilation at moderate excitation fluence in molecular
23
24 systems presenting highly-limited delocalization length have included the random walk motion
25
26 (diffusion) of the excitons before collision and resulting exciton-exciton recombination, at
27
28 moderate excitation fluence.^{11,38} For example, in one-dimensional systems such as linear J-
29
30 aggregates, the bimolecular rate $\beta(t)$ is predicted to have a $t^{-1/2}$ dependency.³⁹ Excitons in 2D
31
32 halide perovskites are expected to be much more spatially delocalized than their counterparts
33
34 in molecular systems. However, due to the ionic nature of the perovskite structure, excitons in
35
36 2D perovskite structures might present reduced delocalization length along the 2D plane
37
38 compared to transition metal dichalcogenides (MoS₂, WSe₂, etc...) or II-VI semiconductors
39
40 such as CdSe. To the best of our knowledge, the effect of the exciton diffusion on the exciton-
41
42 exciton annihilation process in perovskite nanostructures has only been discussed by Li *et al.*
43
44 and Deng *et al.*^{11,12} The former study did not investigate the evolution of the AR times with the
45
46 excitation fluency but extracted the biexciton dynamics from transient absorption
47
48 measurements on $n=5$ CsPbBr₃ NPLs with different lateral areas and found it very fast but
49
50 sensitive to the NPL geometry (recombination time: 14 to 70 ps).¹² The latter work reported a
51
52 transient absorption microscopy study of 2D layered ($n=1$ to 5) perovskite thin films. By
53
54
55
56
57
58
59
60

1
2
3 comparing the diffusion constant and the AR rate extracted from their analysis, the authors
4
5 concluded that the AR is reaction-limited and not diffusion-limited.¹¹
6
7

8
9 Exponential functions are commonly used to fit the AR dynamics.^{7-8,12-13} In the absence of
10 accurate analytical formula to describe the **Equation 1** with time-dependent bimolecular AR
11 rate, we found that the multiexponential fit was adapted to effectively fit the decay traces with
12 high quality. In order to relate the AR rate in s^{-1} extracted from the multiexponential fit with
13 the bimolecular AR rate in cm^2/s , we introduce an effective AR rate, $\tau_{Auger, eff}$, which is the
14 instantaneous rate that can be approximated by using the initial exciton density $\tilde{n}(0)$, according
15 to $\tau_{Auger, eff} = 1/[\beta \times \tilde{n}(0)]$. The effective Auger recombination times are plotted against the initial
16 exciton density for the four NPL samples in **Figure S5** in the SI. It should be noted that $\tau_{Auger, eff}$
17 calculated from β using **Equation 2** cannot be uniquely identified with a specific term in the
18 multiexponential fit. It describes the dynamics occurring over a broad range, from tens to
19 hundreds of picosecond, that are described separately by τ_1 and τ_2 in the case of the
20 multiexponential fit.
21
22
23
24
25
26
27
28
29
30
31
32
33
34
35
36
37



38
39
40
41
42
43
44
45
46
47
48
49
50
51
52
53
54
55
56
57
58
59
60
Figure 3. Evolution of the effective bimolecular AR rate β (black squares) and of the effective linear AR rate constant k_1 (red dots) with the initial exciton density extracted from the TR-PL

1
2
3 decay fit of MAPI $n=3$ NPLs excited at 400 nm. While β decreases with \tilde{n}_0 , the corresponding
4
5 effective linear AR time $\tau_{\text{Auger,eff}} = 1/[\beta \times \tilde{n}(0)]$ follows the same behavior than $\tau_1 = 1/k_1$ (see
6
7 **Figure S5** in the SI).

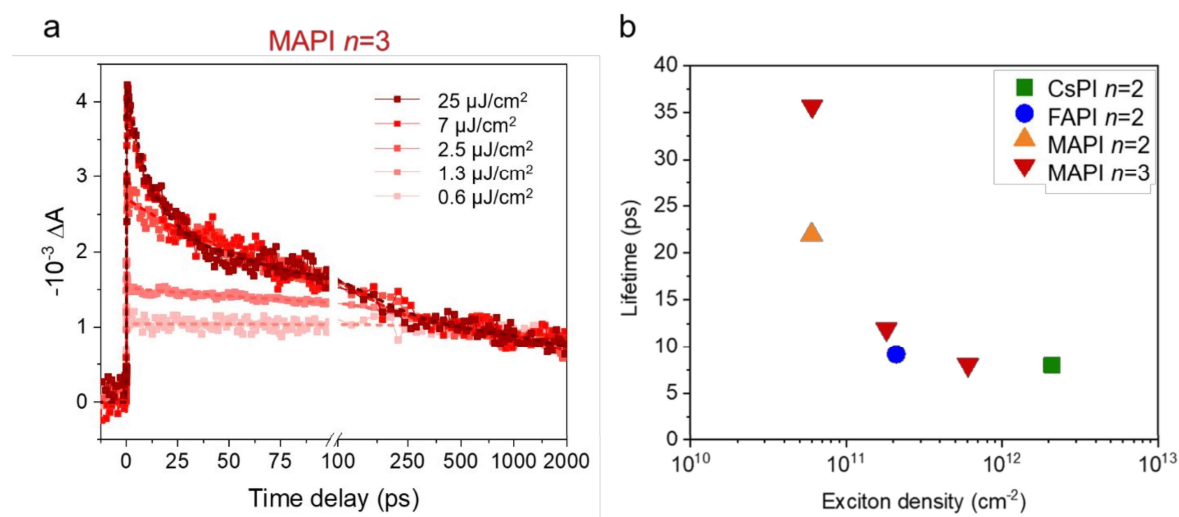
8
9
10 For moderate exciton fluence, the results in **Figure 3** clearly show a diffusion-limited exciton-
11
12 exciton annihilation process with decreasing bimolecular AR rate and increasing corresponding
13
14 linear rate with \tilde{n}_0 . Furthermore, the values of the bimolecular AR rates in the order of 10^{-2}
15
16 cm^2/s are consistent with the exciton diffusion constant reported by Prins *and co.* in the case of
17
18 2D lead iodide perovskite thin film based on butylammonium ligands.⁴⁰ From the trend of the
19
20 *effective* linear and bimolecular AR rates, we found it more appropriate to use the multi-
21
22 exponential fit, clearly showing faster dynamics occurring at larger initial exciton density. We
23
24 further note that the AR time is increasing in NPL samples with larger dimensionality: MAPI
25
26 $n=3$ NPLs seem to present a much-reduced effective linear AR rate than FAPI and MAPI $n=2$
27
28 (**Figure S5**). Moreover, CsPI $n=2$ NPLs presenting a lateral confinement show the fastest AR
29
30 dynamics at low exciton density, *i.e.* this latter sample displays an effective linear rate that is
31
32 less diffusion-limited. We can conclude from these results that the diffusion constant is higher,
33
34 or the exciton wavefunction delocalization in the 2D plane is larger, in more strongly-confined
35
36 NPLs.
37

38
39
40 At higher excitation fluences, τ_1 and the effective AR lifetimes match. However, they attain
41
42 asymptotically a limiting value that is comparable to the temporal resolution of our TCSPC
43
44 setup (IRF about 60 ps). To determine the intrinsic AR rate (*i.e.* not diffusion-limited), we need
45
46 to access the high fluence dynamics with a much higher temporal resolution.
47
48
49

50
51
52 **Visible femtosecond transient absorption (TA).** TA is a spectroscopic technique providing a
53
54 much higher temporal resolution than TCSPC. Excitation fluence-dependent TA experiments
55
56 were carried out on the four NPL samples using band-edge excitation to avoid the effect of
57
58 cooling in the early time dynamics. A detailed description of our TA setup with pump energy
59
60

1
2
3 tunable with a visible non-collinear optical parametric amplifier (NOPA) is given in the
4
5 EXPERIMENTAL SECTION. The NPLs were refreshed within the cuvette using a peristaltic
6
7 pump with adapted tubing to prevent from photo-degradation and photo-charging effects. The
8
9 transient absorption signal ΔA we focus on in this study corresponds to the photo-induced
10
11 bleach (PIB) coming from the saturation of the band-edge transition due to the presence of
12
13 excitons generated by the pump in the lowest energy levels.³²
14
15

16
17 From a global fit analysis of the TA data, we found that the line-shapes were conserved within
18
19 the time-range of interest (ps-ns), including no significant spectral shift in the PIB of the band-
20
21 edge transition (**Figure S6** in SI). Consequently, the kinetic trace at the PIB maximum averaged
22
23 over a few nanometers can be fitted directly. The sign of the negative PIB signal was inverted
24
25 in order to facilitate comparisons with TR-PL analysis and the PIB decays were normalized at
26
27 long time to highlight the extra faster decay component appearing at high excitation fluence.
28
29 The data are shown in **Figure 4a** for MAPI $n=3$ NPLs and **Figure S7** in the SI for the three $n=2$
30
31 NPL samples. Similarly with TR-PL dynamics, the TA decays were fit by a multiexponential
32
33 function. The resulting fit parameters are given in **Table S7-S10** in the SI.
34
35
36
37
38
39
40



1
2
3 **Figure 4. (a)** Band-edge PIB traces of MAPI $n=3$ NPLs normalized at long time for different
4 excitation fluences (squares) and multiexponential fit (dashed lines). **(b)** Early-time AR time
5 constants τ_1 extracted from the TA data of MAPI $n=3$ NPLs at three different fluences and in
6 the highest excitation fluence TA decay traces of MAPI, FAPI, and CsPI $n=2$ NPLs.
7
8
9

10
11
12
13
14
15
16 One kinetic component in the nanosecond time range was enough to fit the traces measured at
17 the lowest excitation fluences (about 0.6-0.7 $\mu\text{J}/\text{cm}^2$), which is in agreement with TR-PL data
18 (see the calculation of the number of excitons and exciton density in **Table S11** in the SI). The
19 long-time constants are consistent with the nanosecond single-exciton recombination times
20 measured in TR-PL for all the samples, even if the total TA time range is much shorter (about
21 2 ns compared to 12 ns for TR-PL). Increasing the excitation fluence to of few $\mu\text{J}/\text{cm}^2$ leads to
22 the appearance of additional faster kinetic components, a first on the order of a few hundreds
23 of ps, and a second as short as sub-10 ps. Both time constants decrease with the excitation
24 fluence. In line with the discussion of the TR-PL data, we assign these faster components to
25 multiexciton processes, notably Auger recombination. However, the very fast (< 60 ps)
26 dynamics could not be determined by TR-PL due to its limited IRF. The short time constants
27 (τ_1) obtained by TA are plotted as a function of the exciton density for the four samples in
28 **Figure 4b**. The isolated τ_1 components tend to the same value for all the measured NPL
29 samples, corresponding to an intrinsic Auger recombination time (not diffusion-limited). This
30 shows that the AR process can be described by a collision process (or a short-range energy
31 transfer) without involving a recombination probability per collision. We further note that this
32 sub-10 ps component is much faster compared to other nanomaterials such as II-VI and III-V
33 semiconductors that typically have an AR time on the order of a few hundreds of picoseconds.
34
35
36
37
38
39
40
41
42
43
44
45
46
47
48
49
50
51
52
53
54
55
56
57
58
59
60
The second time component (τ_2) on the order of hundreds of ps is assigned to a diffusion-limited
Auger recombination process.

1
2
3 To further address how the multiexciton recombination rate depends on the exciton density in
4 the two-dimensional perovskite structures, the corresponding inter-exciton distance d_{x-x} can be
5 calculated. In the case of MAPI $n=3$ NPLs, an additional component with a time constant on
6 the order of hundreds of ps appears at excitation fluences as low as $1.3 \mu\text{J}/\text{cm}^2$, corresponding
7 to an initial exciton density of $3 \times 10^{10} \text{ cm}^{-2}$ (calculation in the SI). This leads to an average
8 inter-exciton distance $d_{x-x} \approx 57 \text{ nm}$ (center to center distance, see SI). In the same manner, we
9 estimated the exciton-exciton distance from the excitation fluence where an ultrafast component
10 as short as 10 ps becomes predominant ($> 40 \%$ in amplitude at $25 \pm 4 \mu\text{J}/\text{cm}^2$). For this initial
11 exciton density of $(6 \pm 2) \times 10^{11} \text{ cm}^{-2}$, $d_{x-x} \approx 13 \text{ nm}$. For this distance only four to six times
12 larger than the exciton Bohr radius a_B reported for MAPbI_3 perovskite ($a_B < 3 \text{ nm}^{41}$), the
13 excitons must overlap spatially as they recombine efficiently. Assuming an isotropic exciton
14 delocalization in the 2D plane, we can estimate the coherent exciton radius a_x (*i.e.* the
15 characteristic size of the extent of delocalization of the exciton center-of-mass motion¹⁸ to be
16 about $d_{x-x,\text{min}}/2 = 6.5 \text{ nm}$. For d_{x-x} much larger than the delocalization length, we can only assume
17 that the multiexciton AR rate is limited by the exciton diffusion in the 2D plane. In that case,
18 the effective AR time depends strongly on the sample geometry. This could explain the range
19 of AR rates reported by Li *et al.* in 5 ML-thick CsPbBr_3 NPLs with different lateral sizes,
20 without the need of invoking a different AR probability per exciton collision.¹² It also means
21 that the mono-exponential decay usually extracted for discrete biexcitonic to mono-excitonic
22 recombination process in semiconductor nanostructures is not the intrinsic biexcitonic rate in
23 anisotropic perovskite samples such as 2D NPLs. The intrinsic AR rate can only be obtained at
24 high excitation fluence where the initial photogenerated excitons overlap before diffusion takes
25 place (reaction-limited AR).
26
27
28
29
30
31
32
33
34
35
36
37
38
39
40
41
42
43
44
45
46
47
48
49
50
51
52
53
54
55

56 **Multiple exciton generation in 2D NPLs.** So far, the exciton-exciton interactions were probed
57 at high excitation fluences, where each absorbed photon creates a unique electron-hole pair and
58
59
60

multiple excitons within a single NPL decay predominantly through the Auger recombination process. We now investigate the case of high photon energy, which can potentially lead to multiexciton generation, even in the case of low excitation fluence.

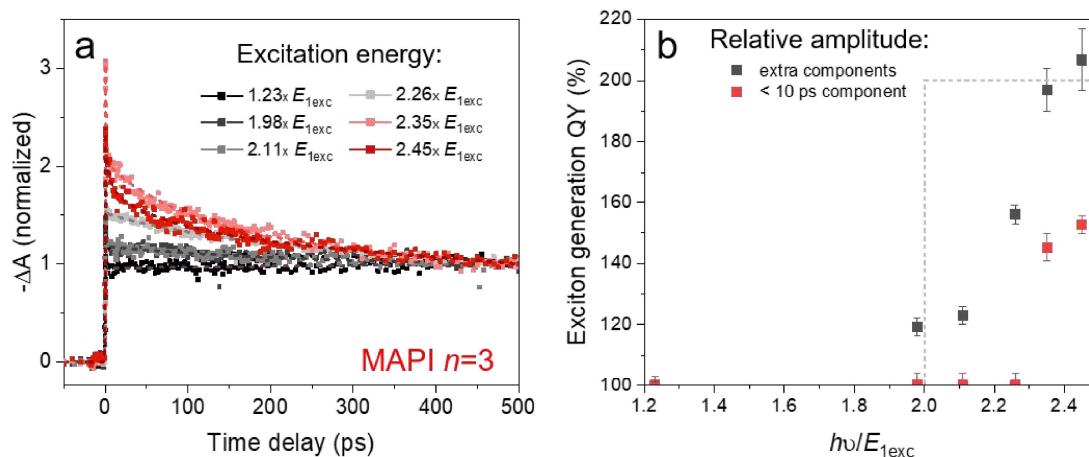


Figure 5. (a) PIB traces at low fluence of MAPI $n=3$ NPLs (band-edge detection, normalized at 500 ps) for different excitation photon energies (corresponding to 500, 310, 290, 270, 260 and 250 nm in wavelength). Experimental data are represented by squares, multi-exponential fits are represented by dashed lines. **(b)** Evolution of the amplitude of the early-time component relative to the single exciton one in MAPI $n=3$ NPLs, including the sub-10 to hundreds of ps components (black squares) and sub-10 ps only (red squares). Dashed grey lines represent the theoretical limit of the maximum quantum yield of generated excitons, 200 %, with an excitation threshold of $2 \times E_{1\text{exc}}$.

We focused the analysis on MAPI $n=3$ NPLs which present the lowest optical bandgap energy ($E_{1\text{exc}} \approx 1.95$ eV) among the four synthesized samples. This allows us to excite the NPLs at various energies E in the ultraviolet (UV), using the second harmonic of the NOPA, well-above (about $2.45 \times E_{1\text{exc}}$, 250 nm) and below (e.g. about 320 nm) the minimum required threshold for MEG ($E = 2 \times E_{1\text{exc}}$). To avoid multiphoton absorption within a single NPLs as far as possible, the excitation pulse energy was decreased to below 1 nJ, while keeping well-behaved

1
2
3 TA dynamics (ΔA from PIB signal around 0.5×10^{-3}). The corresponding exciton density for
4
5 250 nm excitation was for example calculated to be less than 10^{11} cm^{-2} (see SI with the full
6
7 absorption spectrum of the sample **Figure S8**). The extracted PIB dynamics measured at the
8
9 band-edge and normalized at long times are displayed in **Figure 5a** for six different excitation
10
11 wavelengths. The corresponding fit parameters are in the **Table S12** in SI.
12
13

14
15 While for a visible excitation the PIB dynamics can be well described by a mono-exponential
16
17 decay with a long-time component of about 10 ns (represented in black in **Figure 5a**, excitation
18
19 at $1.23 \times E_{1\text{exc}}$ corresponding to 500 nm), extra decay components with time constants ranging
20
21 between few and hundreds of ps emerge for UV excitation. We also observe a coherent artifact
22
23 at times below 300 fs. This is taken into account in the exponential fit but not considered any
24
25 further. Similar to the previous analysis, the faster components can be isolated from the long-
26
27 time single-exciton dynamics after normalization at long times (**Figure S9** in SI). This faster
28
29 dynamics could be interpreted as the indirect observation of MEG, since the excitation fluence
30
31 was reduced to a minimum while exciting the NPLs with high-energy photons. We should note
32
33 that here, per opposition with visible TA experiments, we expected at most two excitons per
34
35 NPL (for low enough excitation fluence). The component characterized by a time constant on
36
37 the order of hundreds of ps is directly observed at relatively low energy excitation ($1.98 \times E_{1\text{exc}}$
38
39 and $2.11 \times E_{1\text{exc}}$) with a relatively low amplitude. However, it becomes much more pronounced
40
41 starting from $2.26 \times E_{1\text{exc}}$ (270 nm in wavelength). At $E \geq 2.35 \times E_{1\text{exc}}$, an additional component
42
43 of a few picoseconds appears. It should be kept in mind that this time constant is much longer
44
45 than the temporal resolution ($< 300 \text{ fs}$ for UV excitation).
46
47
48
49
50

51
52 The sum of amplitudes of the extra dynamics relative to the long one can be plotted versus the
53
54 excitation energy relative to the optical bandgap one ($h\nu/E_{1\text{exc}}$). This leads to an apparent
55
56 number of excitons generated by a single photon (exciton generation quantum yield, QY), seen
57
58 in **Figure 5b** (black squares), as previously reported for perovskite nanocrystals^{14,19} and other
59
60

1
2
3 semiconductor nanostructures.^{42–44} From this plot, it seems that more than one exciton starts to
4
5 be generated just below the theoretical threshold ($1.98 \times E_{1\text{exc}}$) and the maximum MEG
6
7 efficiency (200 %) is reached at $2.45 \times E_{1\text{exc}}$. In the following, we argue that only the fastest
8
9 component of a few picoseconds corresponds to the indirect observation of MEG through the
10
11 resulting fast Auger recombination (red squares **Figure 5b**), while the intermediate component
12
13 with a time constant of hundreds of picoseconds arises from side effects of high excitation
14
15 photon energy.
16
17

18
19 First, several experiments were performed to check that the short picosecond component did
20
21 not arise from a solvent effect. The reason is that toluene starts to absorb light below 290 nm.
22
23 Attempts to re-disperse the $n=3$ NPLs or to synthesize them directly in chloroform (CHCl_3)
24
25 solvent with negligible absorption in the whole UV range of interest, were unsuccessful.
26
27 Nevertheless, liquid scintillation experiments reveal that no emission could be detected from
28
29 the perovskite NPLs after excitation of the toluene molecules, showing the absence of efficient
30
31 energy transfer (see discussion in the SI). Furthermore, the direct synthesis of thinner MAPI
32
33 $n=2$ NPLs in chloroform was possible and TA measurements on this sample do not show any
34
35 picosecond component when exciting at 250 nm, even at higher excitation fluence (**Figure S10a**
36
37 in SI). From our point of view, the MEG threshold was not reached in these materials excited
38
39 under similar conditions to those used for MAPI $n=3$ NPLs, since they have a higher optical
40
41 bandgap.
42
43
44
45
46
47

48
49 Instead, these NPLs show an intermediate component characterized by a time constant on the
50
51 order of hundreds of ps after excitation at 250 nm, but having a much-reduced amplitude
52
53 compared to the same NPLs dispersed in toluene (**Figure S10a** in SI). We interpret this result
54
55 by the enhanced stability of the NPLs in chloroform versus toluene, which leads to a reduction
56
57 of the intermediate component due to non-radiative pathways induced at high photon energy
58
59 exposition. Similarly to the NPL $n=3$ sample in toluene, we found a much higher proportion of
60

1
2
3 this intermediate component when exciting at 250 nm compared to 310 nm (**Figure S10b** in
4 SI). If this component was due to MEG, it would lead to a QY of about 134 % when excited at
5 250 nm (corresponding to an energy of $2.28 \times E_{1\text{exc}}$).
6
7

8
9
10 Reported observations of MEG in colloidal semiconductor nanostructures have often been
11 controversial. That is essentially because the MEG process is not directly observed and the
12 measurements are subject to artefacts, such as photo-charging effects leading to other Auger
13 recombination process (trion-related).⁵ In addition, experiments should be performed as
14 substantially lower excitation fluence to avoid the direct generation of multiple excitons *via*
15 multiphoton absorption. Here, the smooth evolution between 260 and 270 nm of the toluene
16 absorption (**Figure S8**) and of the MAPI $n=3$ NPL absorption cross section, cannot explain why
17 the few picosecond component is only observed at 260 nm under similar excitation condition.
18
19

20 In perovskite NPLs, the strong dependence of the AR rate on the average inter-exciton distance
21 due to the limited exciton delocalization length allows us to unambiguously rule out the
22 possibility that the short ps component could result from an excessive excitation fluence.
23 Indeed, even if the low excitation fluencies used here can still generate more than one exciton
24 per NPL (assuming a Poisson distribution¹⁶), the resulting Auger recombination rate will be at
25 least one order of magnitude slower (diffusion-limited AR, see above). The calculated exciton
26 density obtained for the 250 nm excitation of MAPI $n=3$ NPLs is found to be 10^{11} cm^{-2} at
27 maximum (see SI), which is an order of magnitude lower than the density needed to obtain
28 the sub-10 ps component in the case of one photon generates a single exciton. On the contrary,
29 multiple excitons photogenerated from a *single* high-energy photon will be spatially very close,
30 resulting in a diffusion-less AR time, in the picosecond time range. This is similar to what was
31 measured for high excitation fluence in the visible, when the coherent delocalization areas of
32 two near-lying excitons overlap ($> 25 \mu\text{J}/\text{cm}^2$). The Auger recombination induced by MEG is a
33 reaction of “*geminat*e” biexciton formation (*i.e.* generated directly or indirectly from the same
34
35
36
37
38
39
40
41
42
43
44
45
46
47
48
49
50
51
52
53
54
55
56
57
58
59
60

1
2
3 photon, depending on the mechanism⁴⁵), while at high excitation density, the Auger process is
4
5 due to recombination of excitons generated by the absorption of different photons at distinct
6
7 locations. For nanostructures with a highly delocalized center-of-mass motion wavefunction,
8
9 no clear distinction can be made between the two different origins of the Auger recombination.
10
11 Here, the limited exciton delocalization length in the 2D plane of the perovskite NPLs and their
12
13 highly anisotropic shape allows to isolate the contribution of MEG-induced AR by its
14
15 characteristically fast decay rate. Finally, we can notice that the measured threshold for MEG
16
17 in $n=3$ NPLs is well above the theoretical limit of $2 \times E_{1\text{exc}}$. This can explain why no biexciton
18
19 generation could be observed in the $n=2$ NPL samples with larger confinement effects.
20
21
22

23 24 CONCLUSIONS

25
26
27 The multiple exciton recombination in strongly-confined 2D perovskite NPLs is dominated by
28
29 non-radiative Auger recombination. Due to the large asymmetric geometry of these samples
30
31 and the limited exciton wavefunction delocalization, the Auger recombination rate depends
32
33 strongly on the excitation fluence. At low fluence, when the initial average inter-exciton
34
35 distance is several tens of nanometers, the Auger recombination is limited by exciton diffusion
36
37 and occurs on a timescale of several tens to hundreds of picoseconds. In contrast, high excitation
38
39 fluences produce “overlapping” excitons with inter-exciton distances only a few times the
40
41 exciton Bohr radius, resulting in recombination times of less than 10 ps. This fast rate can
42
43 explain why no efficient lasing could be obtained in these 2D materials. Finally, the dependence
44
45 of the AR rate on the inter-exciton distance allows us to identify the multiexciton dynamics
46
47 resulting from the multiple exciton generation process occurring at high photon energy
48
49 excitation (in the ultraviolet range). For the first time we report the energy threshold of this
50
51 multiple exciton generation in colloidal 2D perovskite NPLs. These findings will hopefully
52
53 contribute to the ongoing research and development of light-emitting devices using 2D
54
55
56
57
58
59
60

1
2
3 perovskite structures. In particular, the fast AR rates and efficient MEG make the NPLs
4
5 promising for applications in single photon sources and photodetectors, respectively.
6
7
8
9
10

11 ASSOCIATED CONTENT

12
13
14
15 **Supporting Information.** This includes the synthesis and characterization of the NPL samples,
16
17 additional TR-PL and TA data, table of the fitting parameters, details of the calculation of the
18
19 exciton density, discussion on the time scale of the radiative biexciton rate and on the liquid
20
21 scintillation experiments. The following files are available free of charge.
22
23
24

25 AUTHOR INFORMATION

26 27 28 **Corresponding Author**

29
30
31 *Corresponding author: elsa.cassette@cea.fr
32
33

34 **ORCID**

35
36
37 Carolina Villamil Franco: 0000-0002-8738-9842
38

39
40
41 Benoît Mahler: 0000-0001-5471-5608
42

43
44
45 Thomas Gustavsson : 0000-0001-7030-6812
46

47
48
49 Elsa Cassette: 0000-0002-1471-6558
50

51 **Notes**

52
53
54 The authors declare no competing financial interest.

55 **Author Contributions**

56
57
58
59
60

1
2
3 The manuscript was written through contributions of all authors. All authors have
4
5
6
7 given approval to the final version of the manuscript.
8
9

10 11 **Funding Sources** 12

13
14 This work was supported by the French Agence Nationale de la Recherche (grant ANR-16-
15
16 ACHN-0022-01).
17

18 19 20 **ACKNOWLEDGMENT** 21

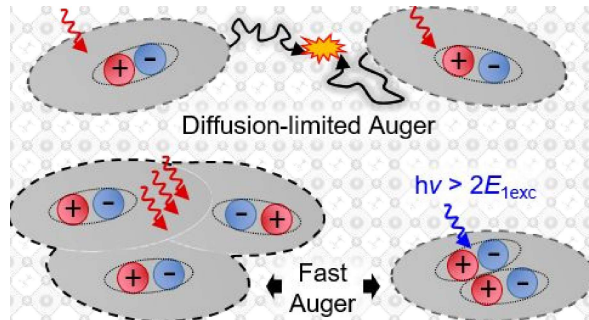
22 E.C. thanks O. Gobert and F. Lepetit for their assistance in the optical and electronic
23
24 development of the TA apparatus. C.V.F. and E.C. thank S. Guizard and D. Markovitsi for
25
26 scientific discussion. C.V.F. and E.C. thank Philippe Cassette for the liquid scintillation
27
28 experiments performed at the LNHB in CEA Saclay. E.C. thanks the ANR program ACHN for
29
30 funding the CaMPUUS project. C.V.F thanks the University Paris-Saclay for the ED 2MIB
31
32 Scholarship. B.M. thanks the Université de Lyon PALSE program (ANR-11-IDEX-0007) and
33
34 C.C. thanks the LabEx PALM of Paris-Saclay University (ANR-10-LABX-0039-PALM), both
35
36 overseen by the ANR under the framework “Investissements d’avenir”.
37
38
39
40

41 42 **ABBREVIATIONS** 43

44
45 AR, Auger recombination; BBO, Ba(BO₂)₂; CCD, charge coupled device; CsPI, cesium lead
46
47 iodide; CW, continuous-wave; FAPI, formamidinium lead iodide; IRF, instrument response
48
49 function; LARP, ligand assisted re-precipitation; LED, electroluminescent diode; MAPI,
50
51 methylammonium lead iodide; MEG, multiple exciton generation; ML, monolayer; NC,
52
53 nanocrystal; NOPA, non-collinear optical parametric amplifier; NPL, nanoplatelet; OD, optical
54
55 density; PIB, photo-induced bleach; QY, quantum yield; TA, transient absorption; TCSPC,
56
57
58
59
60

1
2
3 time-correlated single photon counting; TR-PL, time-resolved photoluminescence; UV,
4
5 ultraviolet; WL, white-light; 2D, two-dimensional.
6
7
8
9
10
11
12
13
14
15
16
17
18
19
20
21
22
23
24
25
26
27
28
29
30
31
32
33
34
35
36
37
38
39
40
41
42
43
44
45
46
47
48
49
50
51
52
53
54
55
56
57
58
59
60

TOC



REFERENCES

- (1) Fu, Y.; Zhu, H.; Chen, J.; Hautzinger, M. P.; Zhu, X. Y.; Jin, S. Metal Halide Perovskite Nanostructures for Optoelectronic Applications and the Study of Physical Properties. *Nature Reviews Materials*. Nature Publishing Group March 2019, pp 169–188.
- (2) Zhang, Q.; Su, R.; Du, W.; Liu, X.; Zhao, L.; Ha, S. T.; Xiong, Q. Advances in Small Perovskite-Based Lasers. *Small Methods* **2017**, *1* (9), 1700163.
- (3) Zhu, H.; Fu, Y.; Meng, F.; Wu, X.; Gong, Z.; Ding, Q.; Gustafsson, M. V.; Trinh, M. T.; Jin, S.; Zhu, X. Lead Halide Perovskite Nanowire Lasers with Low Lasing Thresholds and High Quality Factors. *Nat. Mater.* **2015**, *14* (6), 636–642.
- (4) She, C.; Fedin, I.; Dolzhenkov, D. S.; Demortière, A.; Schaller, R. D.; Pelton, M.; Talapin, D. V. Low-Threshold Stimulated Emission Using Colloidal Quantum Wells. *Nano Lett.* **2014**, *14* (5), 2772–2777.
- (5) Klimov, V. I. Multicarrier Interactions in Semiconductor Nanocrystals in Relation to the Phenomena of Auger Recombination and Carrier Multiplication. *Annu. Rev. Condens. Matter Phys.* **2014**, *5* (1), 285–316.
- (6) Klimov, V. I. Spectral and Dynamical Properties of Multiexcitons in Semiconductor

- 1
2
3 Nanocrystals. *Annu. Rev. Phys. Chem.* **2007**, *58* (1), 635–673.
- 4
5
6 (7) Makarov, N. S.; Guo, S.; Isaienko, O.; Liu, W.; Robel, I.; Klimov, V. I. Spectral and
7
8 Dynamical Properties of Single Excitons, Biexcitons, and Trions in Cesium–Lead-
9
10 Halide Perovskite Quantum Dots. *Nano Lett.* **2016**, *16* (4), 2349–2362.
- 11
12
13 (8) Castañeda, J. A.; Nagamine, G.; Yassitepe, E.; Bonato, L. G.; Voznyy, O.; Hoogland,
14
15 S.; Nogueira, A. F.; Sargent, E. H.; Cruz, C. H. B.; Padilha, L. A. Efficient Biexciton
16
17 Interaction in Perovskite Quantum Dots Under Weak and Strong Confinement. *ACS*
18
19 *Nano* **2016**, *10* (9), 8603–8609.
- 20
21
22 (9) Fang, H.-H.; Protesescu, L.; Balazs, D. M.; Adjokatse, S.; Kovalenko, M. V.; Loi, M.
23
24 A. Exciton Recombination in Formamidinium Lead Triiodide: Nanocrystals versus
25
26 Thin Films. *Small* **2017**, *13* (32), 1700673.
- 27
28
29 (10) Delport, G.; Chehade, G.; Lédeé, F.; Diab, H.; Milesi-Brault, C.; Trippé-Allard, G.;
30
31 Even, J.; Lauret, J. S.; Deleporte, E.; Garrot, D. Exciton-Exciton Annihilation in Two-
32
33 Dimensional Halide Perovskites at Room Temperature. *J. Phys. Chem. Lett.* **2019**, *10*
34
35 (17), 5153–5159.
- 36
37
38 (11) Deng, S.; Shi, E.; Yuan, L.; Jin, L.; Dou, L.; Huang, L. Long-Range Exciton Transport
39
40 and Slow Annihilation in Two-Dimensional Hybrid Perovskites. *Nat. Commun.* **2020**,
41
42 *11* (1), 1–8.
- 43
44
45 (12) Li, Q.; Yang, Y.; Que, W.; Lian, T. Size- and Morphology-Dependent Auger
46
47 Recombination in CsPbBr₃ Perovskite Two-Dimensional Nanoplatelets and One-
48
49 Dimensional Nanorods. *Nano Lett.* **2019**, *19* (8), 5620–5627.
- 50
51
52 (13) Vale, B. R. C.; Socie, E.; Burgos-Caminal, A.; Bettini, J.; Schiavon, M. A.; Moser, J.
53
54 E. Exciton, Biexciton, and Hot Exciton Dynamics in CsPbBr₃ Colloidal Nanoplatelets.
55
56
57
58
59
60

- 1
2
3 *J. Phys. Chem. Lett.* **2020**, 387–394.
4
5
6 (14) Cong, M.; Yang, B.; Chen, J.; Hong, F.; Yang, S.; Deng, W.; Han, K. Carrier
7 Multiplication and Hot-Carrier Cooling Dynamics in Quantum-Confined CsPbI₃
8 Perovskite Nanocrystals. *J. Phys. Chem. Lett.* **2020**, *11* (5), 1921–1926.
9
10
11
12
13 (15) Pelant, I.; Valenta, J. *Luminescence Spectroscopy of Semiconductors*; Oxford
14 University Press: Oxford, 2012; Vol. 9780199588.
15
16
17
18 (16) Klimov, V. I. *Nanocrystal Quantum Dots -2nd Edition*; 2010.
19
20
21
22 (17) Klimov, V. I.; McGuire, J. A.; Schaller, R. D.; Rupasov, V. I. Scaling of Multiexciton
23 Lifetimes in Semiconductor Nanocrystals. *Phys. Rev. B - Condens. Matter Mater. Phys.*
24 **2008**, *77* (19), 195324.
25
26
27
28
29 (18) Li, Q.; Lian, T. Exciton Spatial Coherence and Optical Gain in Colloidal Two-
30 Dimensional Cadmium Chalcogenide Nanoplatelets. *Acc. Chem. Res.* **2019**, *52* (9),
31 2684–2693.
32
33
34
35
36 (19) Li, M.; Begum, R.; Fu, J.; Xu, Q.; Koh, T. M.; Veldhuis, S. A.; Grätzel, M.; Mathews,
37 N.; Mhaisalkar, S.; Sum, T. C. Low Threshold and Efficient Multiple Exciton
38 Generation in Halide Perovskite Nanocrystals. *Nat. Commun.* **2018**, *9* (1), 3–9.
39
40
41
42
43 (20) de Weerd, C.; Gomez, L.; Capretti, A.; Lebrun, D. M.; Matsubara, E.; Lin, J.; Ashida,
44 M.; Spoor, F. C. M.; Siebbeles, L. D. A.; Houtepen, A. J.; Suenaga, K.; Fujiwara, Y.;
45 Gregorkiewicz, T. Efficient Carrier Multiplication in CsPbI₃ Perovskite Nanocrystals.
46 *Nat. Commun.* **2018**, *9* (1), 1–3.
47
48
49
50
51
52 (21) Smith, C.; Binks, D. J. Multiple Exciton Generation in Colloidal Nanocrystals.
53 *Nanomaterials* **2014**, *4*, 19–45.
54
55
56
57
58 (22) Weidman, M. C.; Goodman, A. J.; Tisdale, W. A. Colloidal Halide Perovskite
59
60

- 1
2
3 Nanoplatelets: An Exciting New Class of Semiconductor Nanomaterials. *Chem. Mater.*
4
5 **2017**, *29* (12), 5019–5030.
6
7
8
9 (23) Hintermayr, V. A.; Polavarapu, L.; Urban, A. S.; Feldmann, J. Accelerated Carrier
10 Relaxation through Reduced Coulomb Screening in Two-Dimensional Halide
11 Perovskite Nanoplatelets. *ACS Nano* **2018**, *12* (10), 10151–10158.
12
13
14
15 (24) Levchuk, I.; Osvet, A.; Tang, X.; Brandl, M.; Perea, J. D.; Hoegl, F.; Matt, G. J.; Hock,
16 R.; Batentschuk, M.; Brabec, C. J. Brightly Luminescent and Color-Tunable
17 Formamidinium Lead Halide Perovskite FAPbX₃ (X = Cl, Br, I) Colloidal
18 Nanocrystals. *Nano Lett.* **2017**, *17* (5), 2765–2770.
19
20
21
22
23
24
25 (25) Weidman, M. C.; Seitz, M.; Stranks, S. D.; Tisdale, W. A. Highly Tunable Colloidal
26 Perovskite Nanoplatelets through Variable Cation, Metal, and Halide Composition.
27 *ACS Nano* **2016**, *10* (8), 7830–7839.
28
29
30
31
32
33 (26) Blancon, J. C.; Tsai, H.; Nie, W.; Stoumpos, C. C.; Pedesseau, L.; Katan, C.;
34 Kepenekian, M.; Soe, C. M. M.; Appavoo, K.; Sfeir, M. Y.; Tretiak, S.; Ajayan, P. M.;
35 Kanatzidis, M. G.; Even, J.; Crochet, J. J.; Mohite, A. D. Extremely Efficient Internal
36 Exciton Dissociation through Edge States in Layered 2D Perovskites. *Science* **2017**,
37 *355* (6331), 1288–1292.
38
39
40
41
42
43
44 (27) Paritmongkol, W.; Dahod, N. S.; Stollmann, A.; Mao, N.; Settens, C.; Zheng, S. L.;
45 Tisdale, W. A. Synthetic Variation and Structural Trends in Layered Two-Dimensional
46 Alkylammonium Lead Halide Perovskites. *Chem. Mater.* **2019**, *31* (15), 5592–5607.
47
48
49
50
51
52 (28) Eperon, G. E.; Stranks, S. D.; Menelaou, C.; Johnston, M. B.; Herz, L. M.; Snaith, H. J.
53 Formamidinium Lead Trihalide: A Broadly Tunable Perovskite for Efficient Planar
54 Heterojunction Solar Cells. *Energy Environ. Sci.* **2014**, *7* (3), 982–988.
55
56
57
58
59
60

- 1
2
3 (29) Baghani, E.; O'Leary, S. K.; Fedin, I.; Talapin, D. V.; Pelton, M. Auger-Limited
4 Carrier Recombination and Relaxation in CdSe Colloidal Quantum Wells. *J. Phys.*
5 *Chem. Lett.* **2015**, 150302175751004.
6
7
8
9
10 (30) Johnston, M. B.; Herz, L. M. Hybrid Perovskites for Photovoltaics: Charge-Carrier
11 Recombination, Diffusion, and Radiative Efficiencies. *Acc. Chem. Res.* **2016**, *49* (1),
12 146–154.
13
14
15
16
17 (31) Eperon, G. E.; Jedlicka, E.; Ginger, D. S. Biexciton Auger Recombination Differs in
18 Hybrid and Inorganic Halide Perovskite Quantum Dots. *J. Phys. Chem. Lett.* **2018**, *9*
19 (1), 104–109.
20
21
22
23
24
25 (32) Klimov, V. I. Optical Nonlinearities and Ultrafast Carrier Dynamics in Semiconductor
26 Nanocrystals. *J. Phys. Chem. B* **2000**, *104* (26), 6112–6123.
27
28
29
30 (33) Makarov, N. S.; Guo, S.; Isaienko, O.; Liu, W.; Robel, I.; Klimov, V. I. Spectral and
31 Dynamical Properties of Single Excitons, Biexcitons, and Trions in Cesium–Lead-
32 Halide Perovskite Quantum Dots. *Nano Lett.* **2016**, *16* (4), 2349–2362.
33
34
35
36
37 (34) Binks, D. J. Multiple Exciton Generation in Nanocrystal Quantum Dots - Controversy,
38 Current Status and Future Prospects. *Phys. Chem. Chem. Phys.* **2011**, *13* (28), 12693–
39 12704.
40
41
42
43
44
45 (35) Lakowicz, J. R. *Principles of Fluorescence Spectroscopy*; Springer, 2006.
46
47
48 (36) Kim, M.; Nagirnyi, V.; Feldbach, E.; De Grazia, M.; Carré, B.; Merdji, H.; Guizard,
49 S.; Geoffroy, G.; Gaudin, J.; Fedorov, N.; Martin, P.; Vasil'ev, A.; Belsky, A. Exciton-
50 Exciton Interactions in CdWO₄ Irradiated by Intense Femtosecond Vacuum Ultraviolet
51 Pulses. *Phys. Rev. B - Condens. Matter Mater. Phys.* **2009**, *79* (23), 233103.
52
53
54
55
56
57 (37) Kunneman, L. T.; Tessier, M. D.; Heuclin, H.; Dubertret, B.; Aulin, Y. V.; Grozema, F.
58
59
60

- 1
2
3 C.; Schins, J. M.; Siebbeles, L. D. A. Bimolecular Auger Recombination of Electron-
4 Hole Pairs in Two-Dimensional CdSe and CdSe/CdZnS Core/Shell Nanoplatelets. *J.*
5 *Phys. Chem. Lett.* **2013**, *4* (21), 3574–3578.
6
7
8
9
10
11 (38) Gösele, U. Anisotropic Diffusion, Long-Range Energy Transfer and Bimolecular
12 Exciton Recombination Kinetics. *Chem. Phys. Lett.* **1976**, *43* (1), 61–64.
13
14
15
16 (39) Burgel, M.; Van; Wiersma, D. A. *The Ultrafast Dynamics of Aggregate Excitons in*
17 *Water*; s.n., 1999.
18
19
20
21 (40) Seitz, M.; Magdaleno, A. J.; Alcázar-Cano, N.; Meléndez, M.; Lubbers, T. J.;
22 Walraven, S. W.; Pakdel, S.; Prada, E.; Delgado-Buscalioni, R.; Prins, F. Exciton
23 Diffusion in Two-Dimensional Metal-Halide Perovskites. *Nat. Commun.* **2020**, *11* (1),
24 1–8.
25
26
27
28
29
30
31 (41) Tanaka, K.; Takahashi, T.; Ban, T.; Kondo, T.; Uchida, K.; Miura, N. Comparative
32 Study on the Excitons in Lead-Halide-Based Perovskite-Type Crystals CH₃NH₃PbBr₃
33 CH₃NH₃PbI₃. *Solid State Commun.* **2003**, *127* (9–10), 619–623.
34
35
36
37
38
39 (42) Schaller, R. D.; Agranovich, V. M.; Klimov, V. I. High-Efficiency Carrier
40 Multiplication through Direct Photogeneration of Multi-Excitons via Virtual Single-
41 Exciton States. *Nat. Phys.* **2005**, *1* (3), 189–194.
42
43
44
45
46 (43) Ellingson, R. J.; Beard, M. C.; Johnson, J. C.; Yu, P.; Micic, O. I.; Nozik, A. J.;
47 Shabaev, A.; Efros, A. L. Highly Efficient Multiple Exciton Generation in Colloidal
48 PbSe and PbS Quantum Dots. *Nano Lett.* **2005**, *5* (5), 865–871.
49
50
51
52
53
54 (44) Aerts, M.; Bielewicz, T.; Klinke, C.; Grozema, F. C.; Houtepen, A. J.; Schins, J. M.;
55 Siebbeles, L. D. A. Highly Efficient Carrier Multiplication in PbS Nanosheets. *Nat.*
56 *Commun.* **2014**, *5*, 1–5.
57
58
59
60

1
2
3
4
5
6
7
8
9
10
11
12
13
14
15
16
17
18
19
20
21
22
23
24
25
26
27
28
29
30
31
32
33
34
35
36
37
38
39
40
41
42
43
44
45
46
47
48
49
50
51
52
53
54
55
56
57
58
59
60

- (45) Shabaev, A.; Hellberg, C. S.; Efros, A. L. Efficiency of Multiexciton Generation in Colloidal Nanostructures. *Acc. Chem. Res.* **2013**, *46* (6), 1242–1251.